Nano Research

Open Access

Research Article

Scalable assembly of lightweight electromagnetic wave absorption aerogel via ion crosslinking and ambient pressure drying

Yong Zhang[1] ✉, Qing Zhang[2], Shicheng Wei[2], Fuyao Liu[1], Shilei Zhao[1], Chaohua Xue[3], Ying Zhai[4], Lin Hou[5], Haichao Zhao[2] ✉, Ruidong Shi[2] ✉, and Wei Fan[1] ✉

[1] *Key Laboratory of Functional Textile Material and Product of Ministry of Education, School of Textile Science and Engineering, Xi'an Polytechnic University, Xi'an 710048, China*
[2] *Department of Equipment Maintenance and Remanufacturing Engineering, Army Arms University of PLA, Beijing 100072, China*
[3] *College of Bioresources Chemical and Materials Engineering, Shaanxi University of Science and Technology, Xi'an 710021, China*
[4] *Shaanxi Huaqin Technology Industry Co., ltd., Xi'an 710117, China*
[5] *Shaanxi Yuanfeng Prosafe Co., Ltd., Xi'an 710025, China*

Cite this article: *Nano Research*, **2026**, *19*, 94908376. https://doi.org/10.26599/NR.2026.94908376

ABSTRACT: Electromagnetic wave absorption (EWA) aerogels combine high porosity and large specific surface area, which reduce the effective dielectric constant and improve impedance matching, thereby enhancing EWA capability. However, most reported fabrication strategies rely on complex processes such as supercritical drying or freeze-drying, hindering large-scale production. Achieving both high EWA performance and scalable production remains challenging. Herein, we select carbon nanotubes (CNTs) as the dielectric loss phase, nickel ferrite ($NiFe_2O_4$) as the magnetic loss phase, and cellulose nanofibers (CNFs) as the skeleton to assemble a novelty CNT/$NiFe_2O_4$/CNF (CNC) aerogel through simple solvent exchange, ion crosslinking, and ambient pressure drying. Solvent exchange and Ca^{2+} coordination with carboxyl groups of CNFs and CNTs suppress capillary-induced structural collapse and maintain the porous network of the CNC aerogel during ambient drying. The introduction of CNTs enhances the conductive network and interfacial polarization, while maintaining favourable impedance matching. As the content of CNTs increases, the dielectric constant gradually rises, while the magnetic loss remained stable. The optimized CNC aerogel achieves the reflection loss of −55.62 dB at the frequency of 6.42 GHz with a matching thickness of 2.80 mm, and an effective absorption bandwidth that covers 10.65 GHz at a thickness of 1.53 mm. Radar cross-section simulations further confirmed its potential for practical EWA applications. The assembly strategy provides a scalable route to lightweight, broadband EWA aerogels.

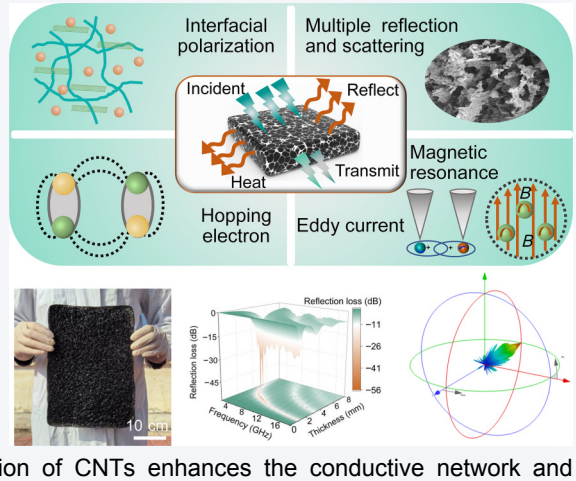

KEYWORDS: aerogels, cellulose, ion crosslinking, ambient pressure drying, electromagnetic wave absorption

1 Introduction

The widespread coverage of 5G technology and intelligent electronic devices has intensified concerns about electromagnetic radiation pollution, which disrupts precision instruments and poses potential health risk [1–5]. Consequently, the development of electromagnetic wave absorption (EWA) materials that combine lightweight, and broadband absorption has been gradually payed attention [6, 7]. Aerogels with porous structure, low density, and high specific surface area, are considered potential matrix for EWA materials [8–10]. Carbon nanomaterials, widely used as dielectric loss, can form efficient conductive network even at low contenting, inducing both conductive loss through electron migration and interfacial polarization loss [11, 12]. Carbon-based aerogels integrate the advantages of porosity, low density, shape adaptability, and high specific surface area [13–17]. These features promote multiple reflections and scattering of electromagnetic waves, effectively reducing the effective dielectric constant [18, 19].

Received: November 3, 2025; **Revised:** December 8, 2025
Accepted: December 26, 2025

✉Address correspondence to Yong Zhang, zhangyong.2019@tsinghua.org.cn; Haichao Zhao, zhchebei@sina.com; Ruidong Shi, srdong1152148048@163.com; Wei Fan, fanwei@xpu.edu.cn

However, their high electrical conductivity can lead to impedance mismatch. Therefore, incorporating magnetic materials into carbon-based aerogels to construct multi-component systems that leverage synergistic dielectric-magnetic loss, thereby optimizing impedance matching and enhancing interfacial polarization [20–25]. The combined approach represents a promising strategy for developing broadband, high-performance electromagnetic wave absorbers.

Despite significant progresses, most aerogel-based absorbers are fabricated using freeze-drying and supercritical drying strategies [26–28]. These methods are effective, but time-consuming, energy-intensive, and the limitations in production scalability [29]. In contrast, ambient pressure drying offers a cost-effective and scalable alternative, as it requires neither specialized equipment nor extreme conditions [30]. However, capillary forces generated during solvent evaporation can cause significant shrinkage, or structural collapse. To overcome these limitations, ion crosslinking strategy has been introduced as an effective means to effectively strengthen networks and suppress shrinkage. Multivalent metal ions such as Ca^{2+} and Al^{3+} can coordinate with carboxyl or hydroxyl groups in polymers, thereby enhancing the rigidity of the gel skeleton [30–32]. In addition, replacing high-surface-tension solvents such as water with low-surface-tension alternatives such as ethanol or n-hexane can reduce capillary forces at the solid-liquid interface, minimizing shrinkage and cracking [33]. Therefore, these strategies could be suitable for the fabrication of structurally robust, high-performance EWA aerogels under ambient conditions.

In this work, a facile approach combining ion crosslinking and ambient pressure drying is proposed to assemble EWA aerogels with synergistic dielectric-magnetic loss characteristics. Cellulose nanofibers (CNFs) construct the three-dimensional (3D) porous framework, while carbon nanotubes (CNTs) and nickel ferrite ($NiFe_2O_4$) nanoparticles provide dielectric loss and magnetic loss properties, respectively. Through the freeze molding, solvent exchange, ion crosslinking, and ambient pressure drying, the CNT/$NiFe_2O_4$/CNF (CNC) aerogel with a stable porous network was obtained. CNTs and $NiFe_2O_4$ were uniformly dispersed on the surface of CNC aerogel, contributing to balance dielectric and magnetic losses. The optimized CNC aerogel demonstrated excellent EWA performance, with a minimum reflection loss of −55.62 dB at 6.42 GHz (matching thickness of 2.8 mm) and an effective absorption bandwidth of 10.65 GHz (matching thickness 1.53 mm). Compared with conventional freeze-drying or supercritical dried aerogels, the innovation of this work lies in combining solvent exchange with Ca^{2+} coordination to suppress capillary collapse during ambient drying, enabling large-scale fabrication without high-energy processes. Unlike previous CNT-ferrite-cellulose systems, the present method simultaneously optimizes network stability, dielectric-magnetic synergy, and manufacturing scalability. The obtained CNC aerogels achieve comparable or superior absorption performance at significantly reduced processing cost, demonstrating a clear advancement over existing fabrication strategies. This work provides a significant potential toward the scalable production of lightweight, broadband, and high-performance EWA aerogels.

2 Experimental

2.1 Preparation of CNC aerogels

$NiFe_2O_4$ nanoparticles (0.4 g) was added into 30 mL 1 wt.% carboxylated CNFs dispersion with content of carboxyl group of 1.5 mmol·g^{-1}, and ultrasonicated in an ice-water bath for 1 h to form a $NiFe_2O_4$/CNF suspension. Subsequently, a predetermined amount of carboxylated CNTs was then introduced into and ultrasonicated for an additional 2 h in an ice-water bath to ensure complete dispersion, yielding a homogeneous CNT/$NiFe_2O_4$/CNF (CNC) suspension. The obtained suspension was poured into a mold and frozen at −40 °C for 4 h until fully solidified. The frozen gels were then immersed in a pre-cooled 1 wt.% $CaCl_2$/ethanol solution for 8 h, during which solvent exchange and Ca^{2+} crosslinking occurred simultaneously. Finally, the wet CNC gel was dried in an oven at 50 °C for 4 h under ambient pressure to obtain the CNC aerogel. For comparison, CNC aerogels with different contents of CNTs were prepared using the same procedure, with only the CNTs concentration adjusted.

2.2 Characterization

The microstructure and morphology of the CNC aerogel were examined using a scanning electron microscope (SEM, Hitachi SU8010) at an acceleration voltage of 5 kV. The crystalline structure and elemental composition were analyzed by X-ray diffraction (XRD, Bruker D8 Advance) and X-ray photoelectron spectroscopy (XPS, Thermo Nexsa). XRD patterns were collected using Cu Kα radiation (λ = 0.154 nm) over a 2θ range from 10° to 80°, with a step size of 0.02° and a scanning speed of 5 °·min^{-1}. Raman spectroscopy (Horiba LabRAM HR) with an excitation wavelength of 532 nm was employed to analyze carbon structural defects in the CNC aerogel within the spectral range of 500–2500 cm^{-1}. Magnetic hysteresis loops at room temperature were measured using a vibrating sample magnetometer (VSM, Lake Shore 8604) under magnetic fields of ±20,000 Oe to determine the saturation magnetization (M_s) and coercivity (H_c). The electromagnetic parameters, complex permittivity and complex permeability, were measured in the 2–18 GHz frequency range via the coaxial method using a vector network analyzer (VNA, Ceyear 3672C). For these tests, the CNC aerogels were impregnated with molten paraffin and maintained at 60 °C for 2 h in an oven, to ensure complete pore infiltration. Based on transmission line theory, the reflection loss characteristics of CNC aerogels with different thicknesses were calculated from the measured electromagnetic parameters.

3 Results and discussion

Figure 1(a) illustrates the fabrication process of CNC aerogel. The combined use of solvent exchange and Ca^{2+} crosslinking effectively preserves the 3D porous architecture, even under ambient pressure drying. During the freezing process, ice crystals nucleate and grow, driving phase separation between the CNFs and water, thereby forming the frozen gel. Then, the frozen gel is immersed into the $CaCl_2$/ethanol solution, and solvent exchange and ion crosslinking occurs simultaneously. The exchange of water with ethanol reduces the surface capillary forces, thereby minimizing capillary stress during subsequent drying [34]. Simultaneously, the ion crosslinking of Ca^{2+} ions with the carboxyl groups of CNFs and CNTs further strengthens the gel network and prevents structural collapse. Finally, the wet ethanol gel is dried under ambient pressure, yielding a stable CNC aerogel with rich porous structure. The obtained CNC aerogels are designated as CNCX, where X represents the mass ratio of CNTs incorporated into the dispersion (Table S1 in the Electronic Supplementary Material (ESM)). The

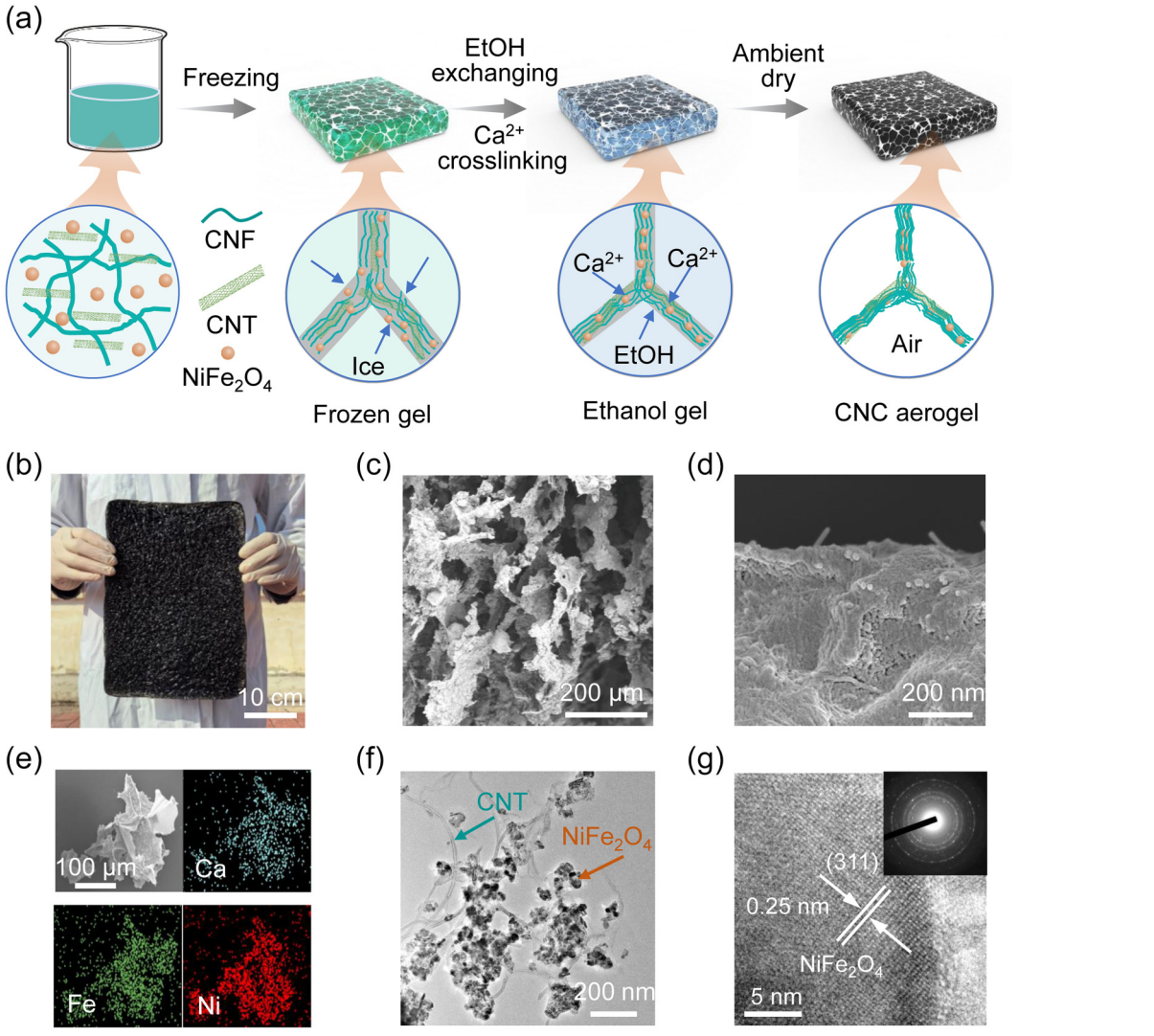

Figure 1 Fabrication, morphology of CNC aerogel. (a) Schematic illustration showing the fabrication process of CNC aerogel. (b) Photograph, (c) SEM image, and (d) magnified SEM image of CNC aerogel. (e) SEM image and corresponding Ca, Fe, and Ni element of CNC aerogel. (f) TEM and (g) HRTEM images of CNC aerogel. The inset in (g) is the corresponding SAED image.

assembly process avoids high-vacuum conditions or specialized drying equipment, offering a simple route to fabricate large-scalable, lightweight CNC aerogels (300 mm × 200 mm × 20 mm, Fig. 1(b)).

The porous structure of the CNC aerogel serves as the foundation for achieving their lightweight characteristics and ability to induce multiple reflections of electromagnetic waves. Compared with the CNC aerogel without ion crosslinking (CNC-0), the Ca^{2+}-crosslinked CNC aerogels exhibit significantly improved stability after ambient pressure drying. CNC-0 suffers severe structural collapse and forms only fragmented, sheet-like residues because capillary forces during water evaporation exceed the mechanical strength (Fig. S1 in the ESM). In contrast, the samples with Ca^{2+} crosslinking (CNC1–CNC4) maintain intact 3D porous structures (Figs. 1(c) and 1(d), and Fig. S2 in the ESM), demonstrating that the combined strategy effectively suppresses structural collapse during ambient drying. Moreover, the combined strategy shows excellent batch-to-batch reproducibility. the controlled freezing rate (uniform freezing at −40 °C) ensures uniform ice crystal growth, and the porosity deviation of aerogels between different batches is ignorable. The ion concentration, dispersion quality and drying conditions are keeping unchanged and do not significantly alter pore morphology. The stable colloidal dispersion of CNFs and the slow ion-exchange rate help minimize fluctuations in network structure, making the process highly tolerant to typical manufacturing variations. Due to structural collapse, CNC-0 exhibits a low porosity of only 42.7% and a high density of 0.186 g·cm^{-3} (Fig. S3 in the ESM), whereas CNC1–CNC4 achieve porosities above 87% and densities between 0.057 to 0.098 g·cm^{-3}, satisfying the lightweight requirement for EWA materials [35]. Elemental mapping images of the CNC aerogel indicate uniform distribution of Ca, Fe, and Ni elements (Fig. 1(e)), confirming the homogeneous dispersion of $NiFe_2O_4$ and CNTs in CNFs matrix. Furthermore, the synergistic effect of the colloidal stability of the CNFs dispersion and ultrasonic treatment yields uniformly distribution of CNTs and $NiFe_2O_4$ nanoparticles (Figs. 1(f) and 1(g)), generating abundant dielectric-magnetic interfaces to enhance the EWA capability [36].

The ion crosslinking between Ca^{2+} and carboxyl groups of CNFs and CNTs, stabilizes the porous network. Thermogravimetric (TG)

curves obtained in N_2 atmosphere shows that the initial weight loss below 150 °C originates from the evaporation of physically adsorbed water. A small amount of moisture is retained within the hydrophilic CNF network even after drying, leading to the observed mass decrease (Fig. 2(a)). Furthermore, the decomposition temperature of CNFs in CNC3 is 15 °C higher than that of CNC1 confirmed by the DTG curves, demonstrating the presence of CNTs and $NiFe_2O_4$ delays decomposition due to enhanced heat dissipation and stronger interfacial bonding. XRD patterns of the CNC aerogels confirm the coexistence of CNFs, $NiFe_2O_4$, and CNTs (Fig. 2(b)). The diffraction peak at 2θ = 22.6° corresponds to the (002) plane of CNFs, while those at 35.9°, 43.7°, and 63.2° correspond to the (311), (400), and (440) planes of $NiFe_2O_4$ (JCPDS 74-2400) [37]. An additional (002) plane of carbon appears at 25°, whose intensity rises with the increasing CNTs content. Raman spectra of CNC aerogels with different content of CNTs are shown in Fig. 2(c). Raman peaks below 1000 cm^{-1} correspond to the characteristic peaks of $NiFe_2O_4$. With the addition of CNTs, CNC2-CNC4 show obvious Raman peaks at 1350 and 1580 cm^{-1}, corresponding to the D peak and G peak of CNTs, respectively. The I_D/I_G ratio can be used to characterize the defect degree of carbon. As the content of CNTs increases, the I_D/I_G slightly increases, which may be mainly due to bond breakage during the ultrasonication and interfacial bonding between CNTs and CNFs, leading to local carbon structure disorder, creating the interface defects. The interface defects act as polarization centers, enhancing the dielectric loss capability.

To further investigate the bonding interactions within the CNC aerogels, Fourier transform infrared (FTIR) spectroscopy and X-ray photoelectron spectroscopy (XPS) characterization are measured. The C=O stretching vibration peak of the carboxyl group shifts from 1628 to 1597 cm^{-1} (Fig. 2(d)), indicating strong electrostatic interactions between the COO^- groups and Ca^{2+} ions. Concurrently, with the addition of CNTs, the O–H stretching vibration peak near 3330 cm^{-1} also redshifts to lower wavenumber and weakens, suggesting abundant hydrogen bonds between CNTs and CNFs that further reinforces structural stability. XPS survey spectra confirm the presence of C, O, Fe, Ni, and Ca elements (Fig. 2(e)). The O 1s XPS spectrum can be deconvoluted into four peaks at 530.4 eV (Fe–O, lattice oxygen from $NiFe_2O_4$), 531.3 eV (C=O from COOH), 532.1 eV (C–O from hydroxyl groups of CNFs), and 532.9 eV (O–H from adsorbed H_2O), respectively (Fig. 2(f)). The deconvolution of C 1s XPS spectrum further reveal changes in the chemical states of carbon (Fig. 2(g), and Figs. S4 and S5 in the ESM). The introduction of CNTs causes the O–C=O peak to shift towards a higher binding energy, confirming that the ion

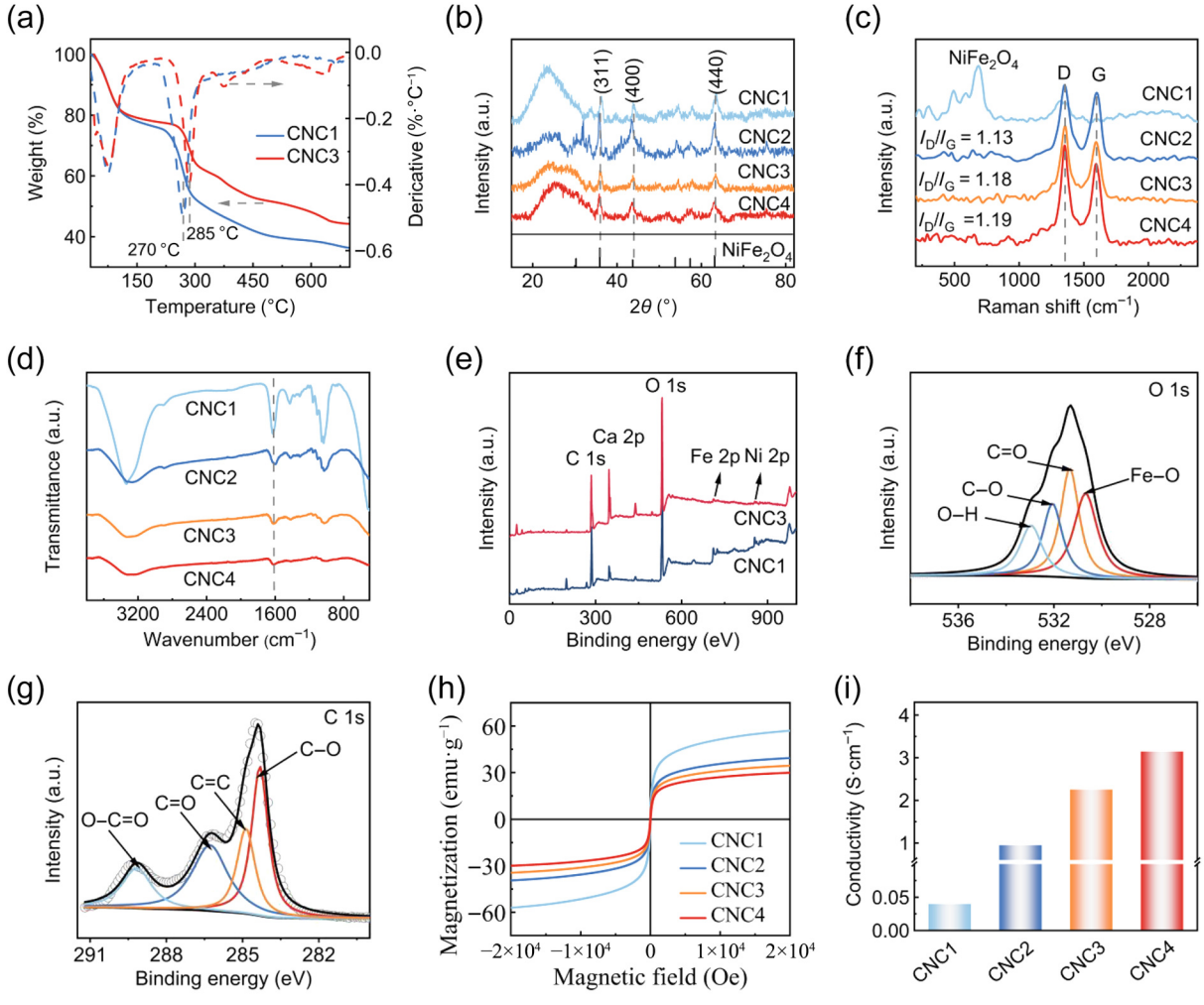

Figure 2 Microstructure of CNC aerogel. (a) TG (solid line) and DTA (dashed line) curves of CNC1 and CNC3 aerogels. (b) XRD pattern, (c) Raman spectra, (d) FTIR spectra, and (e) survey XPS spectra of CNC aerogels. (f) Fe 2p and (g) Ni 2p of CNC3 aerogel. (h) Hysteresis loops of CNC aerogels under the magnetic fields up to 2 × 10^4 Oe. (i) Electrical conductivity of the CNC aerogels.

crosslinking between carboxyl groups and Ca^{2+} ions. The interfacial bonding can promote charge transfer and enhance interfacial polarization loss. Furthermore, the Fe 2p XPS spectrum exhibits spin-orbit doublets at 711.4 eV (Fe^{2+} $2p_{3/2}$) and 724.8 eV (Fe^{3+} $2p_{1/2}$), as well as corresponding satellite peaks, confirm the coexistence of Fe^{2+} and Fe^{3+} mixed valence states (Fig. S6(a) in the ESM). The Fe^{2+}/Fe^{3+} ratio in CNC3 is approximately 1:2, consistent with the spinel $NiFe_2O_4$ structure where Fe^{2+} occupies tetrahedral and Fe^{3+} occupies octahedral sites. The distribution stabilizes magnetic moments, providing magnetic loss while the mixed valence contributes to dipole polarization and additional dielectric loss [38]. The Ni 2p XPS spectra exhibit peaks at 855.0 and 872.5 eV, characteristic of Ni^{2+} $2p_{3/2}$ and Ni^{2+} $2p_{1/2}$, respectively (Fig. S6(b) in the ESM), confirming Ni^{2+} as stable valence. Moreover, CNC0 aerogel exhibits a low specific surface area (SSA) of 10.1 $m^2 \cdot g^{-1}$, while Ca^{2+}-crosslinked CNC1–CNC4 aerogels show much higher SSAs (40.9-83.7 $m^2 \cdot g^{-1}$) with increasing CNTs contents (Fig. S7 in the ESM). Meanwhile, the pore size distribution reveals that CNC0 aerogel has weak pore volume, whereas CNC1–CNC4 aerogels present stronger pore volume with increasing CNTs contents. This indicates Ca^{2+} crosslinking and CNTs incorporation facilitate richer porous structures, benefiting electromagnetic wave absorption via enhanced interfacial polarization. Furthermore, the compressive strength results show that CNC0 aerogel has markedly lower compressive strength than CNC1–CNC4 aerogels. Due to the absence of Ca^{2+} ion, the porous structure of CNC0 aerogel lacks mechanical stability, causing weak loading capacity (Fig. S8 in the ESM). For CNC1–CNC4 aerogels, Ca^{2+} crosslinking and CNTs incorporation enhance structural integrity, yielding higher compressive strength, which is critical for maintaining structural robustness in EWA applications.

Static magnetic and electrical properties determine the balance between magnetic loss and dielectric loss in CNC aerogels. The hysteresis loops of CNC aerogels exhibit a symmetric "S" shaped curves, indicating that CNC aerogels display typical ferromagnetic hysteresis behavior (Fig. 2(h) and Table S2 in the ESM). The saturation magnetization and coercivity of CNC aerogels with different CNTs contents can be calculated from the hysteresis loops. The saturation magnetization of CNC1 reaches to 56.9 emu·g^{-1} and decreases with increasing non-magnetic CNTs content. High saturation magnetization values facilitate stronger electromagnetic energy dissipation. Furthermore, the CNC aerogels exhibit low coercivity of < 90 Oe (Fig. S9 in the ESM), indicating superparamagnetic, which minimizes magnetic hysteresis loss and stabilizes absorption. Additionally, we also measured the electrical conductivity of the CNC aerogels, as shown in Fig. 2(i). Due to the intrinsic non-conductivity of $NiFe_2O_4$ and CNFs, CNC1 exhibits the lowest electrical conductivity, which can limit absorption efficiency due to poor impedance balance. The addition of CNTs increases electrical conductivity and improves dielectric response, optimizing the dielectric-magnetic matching.

According to Maxwell's theory, the EWA capability of CNC aerogels depends on their complex permittivity ($\varepsilon_r = \varepsilon' - j\varepsilon''$) and complex permeability ($\mu_r = \mu' - j\mu''$). Here, ε' and μ′ represent the ability to store electrical and magnetic energy, respectively, while ε'' and μ'' correspond electrical and magnetic losses. The dielectric loss tangent ($\tan\delta_\varepsilon = \varepsilon''/\varepsilon'$) and magnetic loss tangent ($\tan\delta_\mu = \mu''/\mu'$) are used to evaluate the dielectric and magnetic loss capabilities. If $\tan\delta_\varepsilon > \tan\delta_\mu$ at a given frequency range dielectric loss dominates the EWA mechanism of the CNC aerogel, and vice versa. Figure 3 illustrates the frequency-dependent electromagnetic parameters of the CNC aerogels. All ε' values decrease with increasing frequency (Fig. 3(a)), exhibiting typical dielectric dispersion behavior as

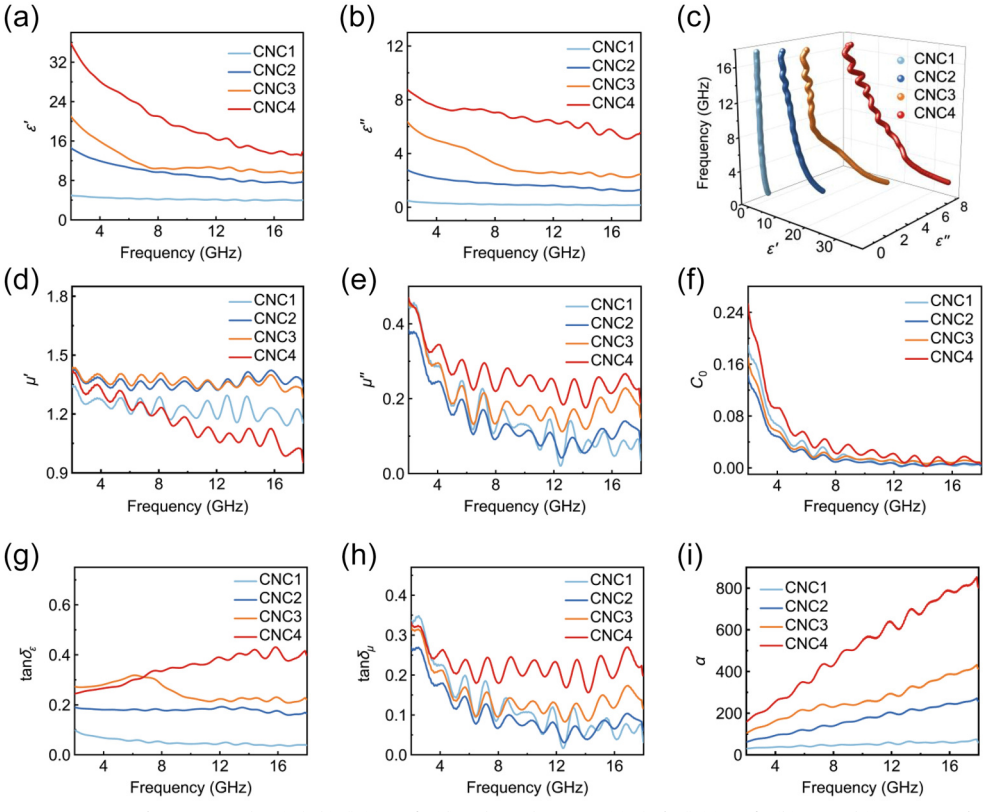

Figure 3 Electromagnetic parameters of CNC aerogels. (a) ε', (b) ε'', (c) $\tan\delta_\varepsilon$, (d) Cole–Cole curves, (e) μ', (f) μ'', (g) $\tan\delta_\mu$, (h) C_0, and (i) α curves of CNC aerogels.

dipoles fail to reorient rapidly enough to follow high-frequency alternating field. CNC1 shows weak dielectric loss due to the large amount of air and the non-conductive CNFs framework, which reduce effective permittivity. The introduction of CNTs enhances charge storage capacity and dielectric loss. As the CNTs content increases, the electrical conductivity of the CNC aerogel improves, leading to a significant rise in ε' and ε'' (Fig. 3(b)). The enhanced dielectric response arises from the more complete conductive network, which facilitates charge transport. Furthermore, CNC aerogels with higher CNTs content exhibit a more noticeable decline in ε', attributed to the presence of more polarizable molecules and free electrons. The dominant polarization mechanisms in the CNC aerogels may include interfacial polarization at heterogeneous boundaries and dipole polarization from structural defects acting as polarization centers. Therefore, increasing the CNTs content can effectively strengthens the dielectric loss behavior of the CNC aerogels. However, excessive CNTs can cause agglomeration, reducing the number of effective interfaces and hindering charge migration, thereby weakening interfacial polarization. The dielectric loss behavior is further analyzed using Debye theory (Eq. (1)). The Cole–Cole curve performs semicircles and tail lines, correspond to polarization relaxation and electronic conduction loss, respectively. Each Debye semicircle represents a relaxation process. As CNTs content increases, the number of Debye semicircles gradually increases due to the multiple interfaces formed among CNFs, CNTs, and $NiFe_2O_4$ and space charge accumulation, which enhances the interfacial polarization (Fig. 3(c)). Additionally, the tail lines of CNC aerogels containing CNTs are longer than that of CNC1, attributing to resulting the electronic conductivity loss.

$$\left(\varepsilon' - \frac{\varepsilon_s + \varepsilon_\infty}{2}\right)^2 + (\varepsilon'')^2 = \left(\frac{\varepsilon_s - \varepsilon_\infty}{2}\right)^2 \quad (1)$$

The dielectric properties of CNC aerogels are jointly regulated by the conductivity of the CNT network and porosity. As the CNT loading increases from CNC1 to CNC4, the formation of more continuous conductive bridges lowers the electron hopping barrier, thereby increasing σ and amplifying the conduction loss. Meanwhile, the high porosity (> 87%) in CNC1–CNC4 suppresses the effective permittivity by introducing abundant air phases. However, the gradual decrease in porosity with increasing CNT content moderately enhances the real part of permittivity because the solid fraction contributes more strongly to charge storage. This dual influence of conductivity and porosity enables tunable dielectric responses. A more conductive but slightly denser framework promotes interfacial polarization and conduction loss, while excessive CNTs shift the system toward impedance mismatch due to over-enhanced permittivity. Therefore, both conductivity and porosity synergistically determine the dielectric relaxation and loss mechanisms in CNC aerogels.

The complex permeability (μ' and μ'') of the CNC aerogels is shown in the Figs. 3(d) and 3(e). A slight increase in μ' is observed for CNC2 and CNC3, which may be attributed to the enhanced induced magnetic field strength associated with improved electrical conductivity. Both μ' and μ'' exhibit frequency-dependent dispersion, primarily due to natural resonance and exchange resonance within the aerogels. The magnetic loss mechanisms include contributions from natural resonance and exchange resonance and eddy current losses. The eddy current loss can be evaluated using the eddy current coefficient (C_0). When magnetic loss is dominated by eddy current, C_0 remains constant with frequency. As seen in Fig. 3(f), distinct resonance peaks in the low-frequency region originate from the natural resonance of $NiFe_2O_4$. With the increasing frequency, C_0 gradually decreases and stabilizes, accompanied by minor resonance peaks, indicating that eddy current loss and exchange resonance dominate the magnetic loss in the medium to high-frequency range. Moreover, the electromagnetic wave absorption of the CNC aerogels arises from the combined effects of dielectric and magnetic losses. Comparison of the frequency-dependence loss tangents shows that $\tan\delta_\mu$ consistently exceeds $\tan\delta_\varepsilon$ across the entire frequency band for CNC1 (Figs. 3(g) and 3(h), and Fig. S10 in the ESM), indicating magnetic loss dominance. With the addition of CNTs, $\tan\delta_\mu$ remains higher than $\tan\delta_\varepsilon$ in the low-frequency range, but $\tan\delta_\varepsilon$ surpasses than $\tan\delta_\mu$ at higher frequency range, signifying a shift towards dielectric loss dominance. Therefore, the CNTs content determines the dominant loss mechanism transitioning from primarily magnetic loss to dielectric loss as the CNTs content increases.

For an ideal EWA material, incident waves should penetrate the material and be dissipated through multiple energy loss pathways. The microwave attenuation constant (α) is often used to evaluate the ability to attenuate electromagnetic waves, where a higher α value indicates stronger attenuation capability. As shown in Fig. 3(i), the α value increases with increasing frequency, demonstrating that the CNC aerogels exhibit enhanced attenuation at higher frequencies. Furthermore, the α value gradually increases with higher CNTs loading, indicating that CNTs significantly enhance the attenuation capability of the CNC aerogels. However, excessively high α values may impair impedance matching, thereby reducing overall absorption efficiency.

According to the transmission line theory, the reflection loss (RL) value and its efficiency can be calculated using Eqs. (2) and (3) [4].

$$RL = 20\lg\left|\frac{Z_{in} - 1}{Z_{in} + 1}\right| \quad (2)$$

$$Z_{in} = Z_0\sqrt{\frac{\mu_r}{\varepsilon_r}}\tanh\left[j\left(\frac{2\pi fd}{c}\right)\sqrt{\mu_r\varepsilon_r}\right] \quad (3)$$

where Z_{in} represents the characteristic impedance of the material surface, Z_0 represents the free space impedance, f, c, and d represent microwave frequency, light speed, and thickness, respectively. The electromagnetic wave absorption performance of CNC aerogel was evaluated by RL and effective absorption bandwidth (EAB, frequency range for RL < −10 dB).

Figure 4 presents the RL curves of the CNC aerogels. For CNC1, at a matching thickness of 7.8 mm, the RL_{min} and EAB are only −20.39 dB and 1.39 GHz, respectively. The introduction of CNTs has obvious effects on the EMW absorption capability. CNC2 achieves an RL_{min} and EAB are −54.14 dB and 2.66 GHz at matching thicknesses of 6.15 mm and 4.15 mm, respectively. CNC3 performs the best absorption intensity with an RL_{min} of −55.62 dB at the frequency of 6.42 GHz with a matching thickness of 2.80 mm and EAB of 5.14 GHz at 1.38 mm. CNC4 exhibits the widest EAB, achieving a broad EAB of 10.65 GHz at a matching thickness of only 1.53 mm, along with an RL_{min} of −25.53 dB at 8.07 GHz with a matching thickness of 2.00 mm. Overall, the EAB gradually broadens as CNTs content increases, while RL_{min} initially improves and then decreases. This trend may be attributed to the continuous

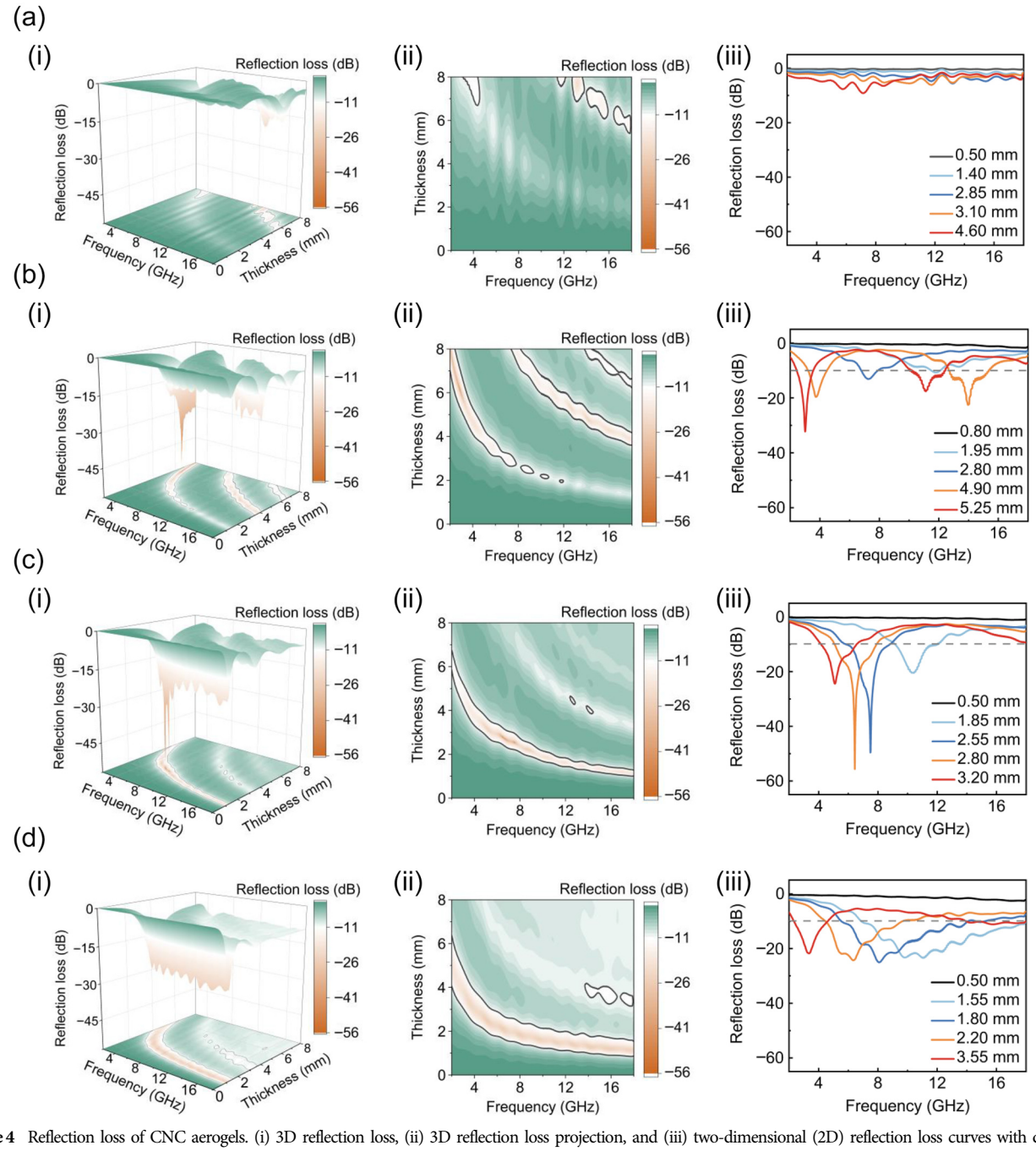

Figure 4 Reflection loss of CNC aerogels. (i) 3D reflection loss, (ii) 3D reflection loss projection, and (iii) two-dimensional (2D) reflection loss curves with different thicknesses of (a) CNC1, (b) CNC2, (c) CNC3, and (d) CNC4 aerogel.

enhancement of the dielectric loss capability, thereby improving wave absorption. However, excessive CNTs lead to impedance mismatch, weakening the EWA performance. Thus, CNTs content plays a crucial role in balancing dielectric and magnetic losses to optimize the EWA behavior of the CNC aerogels.

Based on the above analyses, we propose the EWA mechanism of the CNC aerogels (Fig. 5(a)). Firstly, the abundant porous structure promotes multiple reflections of incident electromagnetic waves within the channels, prolonging the propagation path. Simultaneously, $NiFe_2O_4$ nanoparticles on the pore walls further scatter the waves, increasing interaction time with the absorbing medium. Meanwhile, the continuous conductive CNTs network enables directional free electron transport under alternating electric field, generating Joule heat and resulting in conductive loss. Furthermore, the numerous heterogeneous interfaces among CNTs, $NiFe_2O_4$, and CNFs induce interfacial polarization relaxation, enhancing the dielectric loss. Moreover, the dielectric loss transitions from dipole-dominated relaxation to conduction-dominated pathways as CNT content increases. The ε'' increases almost linearly with measured conductivity, indicating that hopping conduction and tunneling conduction play key roles at higher CNT contents. Meanwhile, magnetic loss remains relatively stable because $NiFe_2O_4$ content is constant. The $NiFe_2O_4$ imparts magnetic loss capability, primarily arising from eddy current loss, natural resonance, and exchange resonance. Thus, higher CNT content deviates the dielectric-magnetic balance, leading to over-

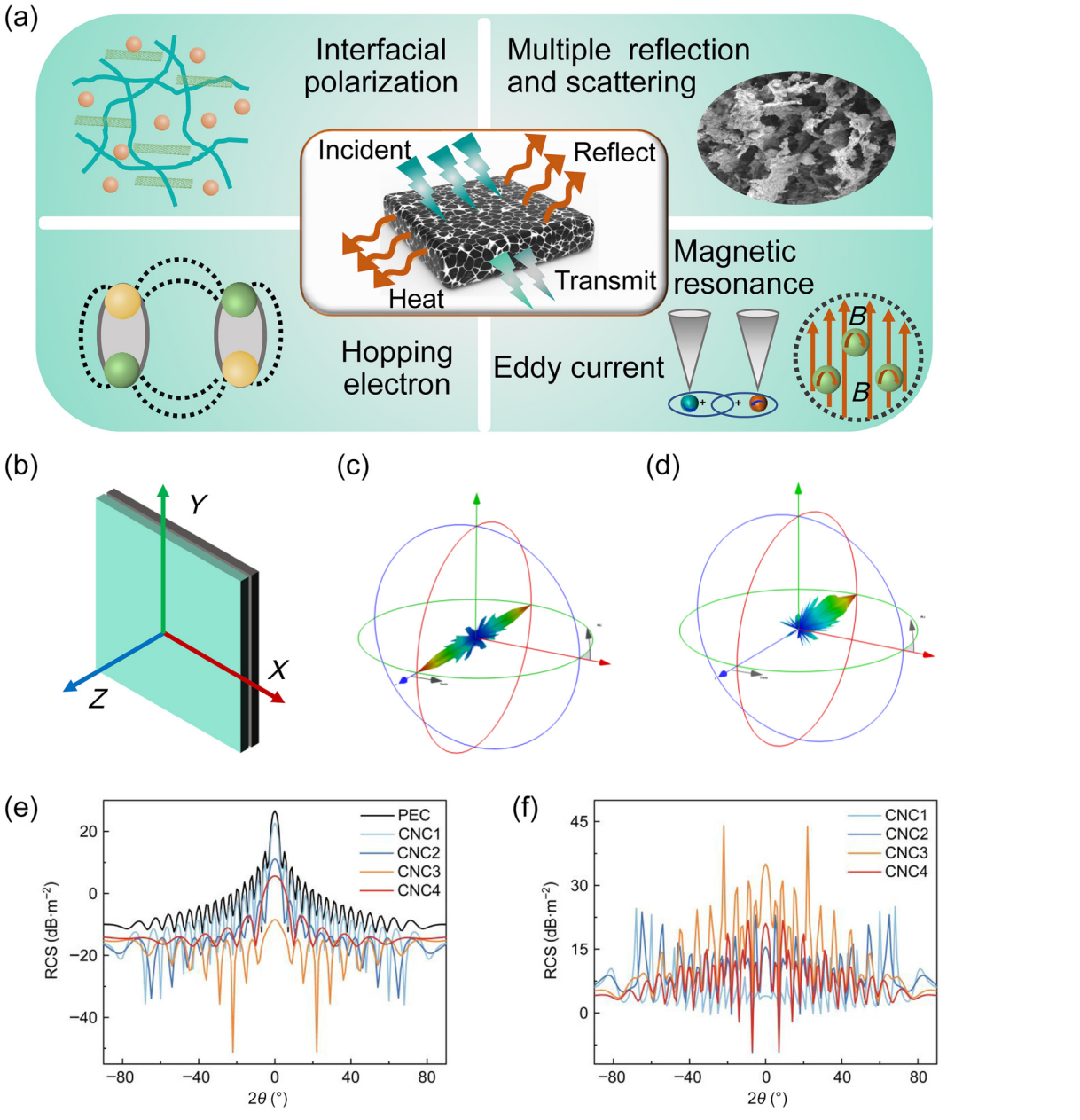

Figure 5 (a) Schematic diagram of the EMW absorption mechanism for CNC aerogel. (b) The RCS simulation model. 3D radar scattering singles of (c) PEC and (d) CNC3 aerogel. (e) RCS curves and (f) efficient RCS reduction values of CNC aerogels.

enhanced ε' and reduced impedance matching. This explains why CNC4 exhibits the widest bandwidth but a reduced RL_{min}. Consequently, the synergistic coupling of dielectric loss and magnetic loss, together with effective impedance matching, endows the CNC aerogels with strong, broadband EWA capability, and being better than most reported EWA materials (Table S3 in the ESM).

To further evaluate the microwave absorption performance of the CNC aerogels, radar cross-section (RCS) simulations were conducted using electromagnetic modeling method (Fig. 5(b)). Both bare PEC and CNC aerogels-coated PEC exhibited distinct radar scattering intensities (Figs. 5(c) and 5(d), and Fig. S11 in the ESM). The bare PEC exhibits the strongest scattering signal, while the PEC coated with the CNC3 aerogel significantly reduces the vertical reflection signal intensity, indicating the excellent radar attenuation capability. A comparative analysis of the RCS reduction of the PEC and the CNC aerogel on the x–o–z plane within a scattering angle range of −90° to 90° reveals that the CNC3 reduces the RCS of the PEC from 26.2 dB·m^{-2} to −8.6 dB·m^{-2}, corresponding to an effective RCS reduction of 34.8 dB·m^{-2} (Fig. 5(e)). Furthermore, except at the 0° direction angle, the CNC3 also exhibits the highest radar scattering reduction at other angles (Fig. 5(f)). Particularly, at a direction angle of 22°, the effective RCS of the CNC3 reaches to 44.1 dB·m^{-2}, confirming its capability to effectively attenuate EMW reflection and scattering from the PEC surface.

4 Conclusion

In summary, lightweight CNC aerogels with abundant porous

structures were successfully assembled through a simple process combining solvent exchange, Ca^{2+} crosslinking, and ambient pressure drying. The synergistic effects of solvent exchange and ion crosslinking between Ca^{2+} and carboxyl groups effectively prevented structural collapse induced by capillary forces during ambient drying. The addition of CNTs significantly enhanced the EWA performance of the CNC aerogels by introducing abundant heterogeneous interfaces among CNTs, $NiFe_2O_4$, and CNFs. The interfaces promoted conductive loss, dipole polarization, and interfacial polarization, while the rich porous structure prolonged the propagation path of incident electromagnetic waves, reinforcing both dielectric and magnetic losses. The CNT content and matching thickness were identified as key factors governing the EWA capability of the CNC aerogels. The optimized CNC aerogel achieved a RL_{min} of −55.62 dB at a thickness of 2.80 mm, demonstrating efficient impedance matching and balanced dielectric and magnetic losses. Owing to the ambient-pressure drying and ion-crosslinking strategy, the CNC aerogels can be fabricated in centimeter- to decimeter-scale batches, demonstrating strong potential for practical deployment. Their lightweight nature and flexibility in thickness design enable integration into the radomes of unmanned aerial vehicles, electromagnetic shielding layers of intelligent equipment, and large-area absorbing panels for 5G base stations. Furthermore, the mechanical robustness provided by Ca^{2+} coordination and the abundant dielectric–magnetic interfaces allow long-term operational stability under vibration, temperature fluctuations, and bending deformation. These characteristics make CNC aerogels promising candidates for next-generation lightweight stealth coatings and wearable electromagnetic protection devices.

Electronic Supplementary Material: Supplementary material (photographs, SEM image, density and porosity, XPS spectra, magnified hysteresis loops, loss tangent, and 3D radar scattering singles of CNC aerogels) is available in the online version of this article at https://doi.org/10.26599/NR.2026.94908376.

Data availability

All data needed to support the conclusions in the paper are presented in the manuscript and the Electronic Supplementary Material. Additional data related to this paper may be requested from the corresponding author upon request.

Acknowledgements

This work was financially supported by the National Natural Science Foundation of China (No. 22305268).

Declaration of competing interest

All the contributing authors report no conflict of interests in this work.

Author contribution statement

Y. Z.: Writing – review & editing, writing – original draft, funding acquisition, project administration. Q. Z., S. C. W., C. H. X., L. H., S. L. Z., and F. Y. L.: Writing – review & editing, writing – original draft, investigation, conceptualization. Y. Z., H. C. Z., R. D. S., and W. F.: Writing – review & editing, writing – original draft.

Use of AI statement

None.

References

[1] Cheng, Z.; Wang, R. F.; Cao, Y. S.; Cai, Z. H.; Zhang, Z. W.; Huang, Y. Intelligent off/on switchable microwave absorption performance of reduced graphene oxide/VO_2 composite aerogel. *Adv. Funct. Mater.* **2022**, *32*, 2205160.

[2] Ding, J. W.; Shi, R. R.; Gong, C. C.; Wang, C. X.; Guo, Y.; Chen, T.; Zhang, Y. J.; Cong, H. W.; Shi, C. S.; He, F. Defect engineering activates schottky heterointerfaces of graphene/$CoSe_2$ composites with ultrathin and lightweight design strategies to boost electromagnetic wave absorption. *Adv. Funct. Mater.* **2023**, *33*, 2305463.

[3] Huang, W. H.; Song, M.; Wang, S.; Wang, B. K.; Ma, J. C.; Liu, T.; Zhang, Y. N.; Kang, Y. F.; Che, R. C. Dual-step redox engineering of 2D coni-alloy embedded B, N-doped carbon layers toward tunable electromagnetic wave absorption and light-weight infrared stealth heat insulation devices. *Adv. Mater.* **2024**, *36*, 2403322.

[4] Isari, A. A.; Ghaffarkhah, A.; Hashemi, S. A.; Wuttke, S.; Arjmand, M. Structural design for EMI shielding: From underlying mechanisms to common pitfalls. *Adv. Mater.* **2024**, *36*, 2310683.

[5] Sun, Y.; Zhang, Y.; Shi, H. Y.; Wang, S. J.; Liu, J. J.; Luo, Y.; Zhang, C.; Zhang, K.; Li, S. X.; Fan, W. Hierarchically engineered flame-retardant triboelectric yarn exhibiting robust mechanical performance and humidity-boosted electrical output for firefighting applications. *Adv. Sci.* **2025**, *12*, e07673.

[6] Wang, H. Y.; Hu, P. F.; Sun, X. B.; Hou, Z. L.; Zhao, P. Y.; Zhou, L.; Yang, S. H.; Geng, C. Y.; Zhu, Y. F.; Wu, X. J. et al. Bioinspired disordered aerogel for omnidirectional terahertz response. *Adv. Mater.* **2025**, *37*, 2418889.

[7] Xiong, X.; Jiang, S. C.; Hu, Y. H.; Peng, R. W.; Wang, M. Structured metal film as a perfect absorber. *Adv. Mater.* **2013**, *25*, 3994–4000.

[8] Hou, X. B.; Chen, J.; Chen, Z. L.; Yu, D. Q.; Zhu, S. W.; Liu, T.; Chen, L. M. Flexible aerogel materials: A review on revolutionary flexibility strategies and the multifunctional applications. *ACS Nano* **2024**, *18*, 11525–11559.

[9] Zhang, F.; Li, N.; Shi, J. F.; Xu, L.; Jia, L. C.; Wang, Y. Y.; Yan, D. X. Recent progress on carbon-based microwave absorption materials for multifunctional applications: A review. *Compos. Part B: Eng.* **2024**, *283*, 111646.

[10] Ding, H.; Hu, B.; Wang, Y.; Du, Y. C. Current progress and frontiers in three-dimensional macroporous carbon-based aerogels for electromagnetic wave absorption: A review. *Nanoscale* **2024**, *16*, 21731–21760.

[11] Liu, Z.; Wang, B.; Wei, S. C.; Huang, W.; Wang, Y. J.; Liang, Y. Review of three-dimensional graphene and related composite materials for microwave absorption. *ACS Appl. Nano Mater.* **2024**, *7*, 6772–6784.

[12] Jia, Z. R.; Sun, L. F.; Gao, Z. G.; Lan, D. Modulating magnetic interface layer on porous carbon heterostructures for efficient microwave absorption. *Nano Res.* **2024**, *17*, 10099–10108.

[13] Fu, K. L.; Zhao, J. B.; Liu, F.; Wu, L. L.; Jin, Z. D.; Yang, Y. F.; Qiao, J.; Wang, Z.; Wang, F. L.; Liu, J. R. Enhanced electromagnetic wave absorption of nitrogen-doped reduced graphene oxide aerogels with $LaFeO_3$ cluster modifications. *Carbon* **2023**, *210*, 118071.

[14] Han, X. J.; Feng, Y. F.; Zhang, N.; Du, W.; Zhang, W. L.; Yu, Q. Q.; Liu, Y. F.; Wang, B.; Jiang, F. Y.; Liu, L. Y. et al. Bio-based multifunctional carbon aerogels for ultrawide electromagnetic wave absorption and thermal insulation. *Carbon* **2025**, *238*, 120231.

[15] Jamali, S. B.; Qamar, T. H.; Hassan, S. U.; Ahmed, N.; Ali, F.; Ahmad, S.; Huang, S. X.; Deng, L. W. Microwave absorption of the synthesized 3D Ni@N-doped porous carbon foams for relatively low frequency range. *Carbon* **2025**, *243*, 120498.

[16] Li, J. J.; Yang, S.; Jiao, P. Z.; Peng, Q. Y.; Yin, W. L.; Yuan, Y.; Lu,

H. B.; He, X. D.; Li, Y. B. Three-dimensional macroassembly of hybrid c@cofe nanoparticles/reduced graphene oxide nanosheets towards multifunctional foam. *Carbon* **2020**, *157*, 427–436.

[17] Zhang, G.; Liu, J. L.; Miao, Y. P.; Ge, S. B.; Rezakazemi, M.; Chang, R. H.; Zhang, X. L.; Li, Y.; Fan, W. Advances in controllable water transport of textile porous materials: Mechanism, structure design, fabrication and application. *Adv. Fiber Mater.* **2025**, *7*, 981–1009.

[18] Qiao, J.; Song, Q. H.; Zhang, X.; Zhao, S. Y.; Liu, J. R.; Nyström, G.; Zeng, Z. H. Enhancing interface connectivity for multifunctional magnetic carbon aerogels: An *in situ* growth strategy of metal-organic frameworks on cellulose nanofibrils. *Adv. Sci.* **2024**, *11*, 2400403.

[19] Cao, Y. S.; Cheng, Z.; Wang, R. F.; Liu, X. Y.; Zhang, T. R.; Fan, F.; Huang, Y. Multifunctional graphene/carbon fiber aerogels toward compatible electromagnetic wave absorption and shielding in gigahertz and terahertz bands with optimized radar cross section. *Carbon* **2022**, *199*, 333–346.

[20] Fu, H. D.; Xie, Y.; Chen, R.; Qin, W. Z.; Wang, X.; Qin, Y. Multifunctional integrated CNTs/Si–Zr hybrid phenolic aerogel composites with excellent thermal protection and microwave absorbing properties. *Ceram. Int.* **2025**, *51*, 40512–40522.

[21] Song, M. J.; Yan, L. W.; Li, Y. F.; Jiang, J. P.; Gong, Z. H.; Guo, A. R.; Du, H. Y.; Liu, J. C. Thermal insulated C/SiC nanofiber aerogel with high thermal stability and superior electromagnetic wave absorption performance. *Ceram. Int.* **2024**, *50*, 28907–28917.

[22] Su, X. G.; Wang, J.; Zhang, X. X.; Huo, S. Q.; Chen, W.; Dai, W.; Zhang, B. One-step preparation of $CoFe_2O_4$/FeCo/graphite nanosheets hybrid composites with tunable microwave absorption performance. *Ceram. Int.* **2020**, *46*, 12353–12363.

[23] Gao, Y.; Lei, Z. K.; Pan, L. N.; Wu, Q.; Zhuang, X. H.; Tan, G. G.; Ning, M. Q.; Man, Q. K. Lightweight chitosan-derived carbon/rGO aerogels loaded with hollow $Co_{1-x}Ni_xO$ nanocubes for superior electromagnetic wave absorption and heat insulation. *Chem. Eng. J.* **2023**, *457*, 141325.

[24] Li, Y.; Meng, F. B.; Mei, Y.; Wang, H. G.; Guo, Y. F.; Wang, Y.; Peng, F. X.; Huang, F.; Zhou, Z. W. Electrospun generation of $Ti_3C_2T_x$ MXene@graphene oxide hybrid aerogel microspheres for tunable high-performance microwave absorption. *Chem. Eng. J.* **2020**, *391*, 123512.

[25] Deng, L. L.; Zhang, J. B.; Shu, R. W. Fabrication of three-dimensional nitrogen-doped reduced graphene oxide/Tin oxide composite aerogels as high-performance electromagnetic wave absorbers. *J. Colloid Interface Sci.* **2021**, *602*, 282–290.

[26] Zhang, B.; Qu, Z. Y.; Ruiz-Agudo, C.; Yang, L.; Chi, B. H.; Kong, Y.; Wang, F. Z. Lightweight magnetic carbon nanotube/cellulose nanofibre aerogels with microstructure engineering for enhanced microwave absorption. *Carbon* **2025**, *234*, 120020.

[27] Du, L. F.; Li, Y. K.; Zhou, Q.; Zhang, L. Q.; Shi, T. T.; Wang, X. L.; Zhang, J. S.; Zhao, J.; Wang, J.; Fan, X. M. Facilitative preparation of graphene/cellulose aerogels with tunable microwave absorption properties for ultra-lightweight applications. *J. Colloid Interface Sci.* **2025**, *679*, 987–994.

[28] Xiao, H.; Yi, M. Y.; Zhao, X.; Chen, M. H.; He, X.; Tan, W.; Yang, W. J.; Zeng, K.; Hu, J. H.; Yang, G. Ultrasound-assisted freeze-drying graphitization process for the fabrication of two-dimensional carbon/Fe_3O_4 composite aerogels for microwave absorption. *Mater. Today Commun.* **2024**, *41*, 110711.

[29] Xiong, C. Y.; Wang, T. X.; Zhang, Y. K.; Zhu, M.; Ni, Y. H. Recent progress on green electromagnetic shielding materials based on macro wood and micro cellulose components from natural agricultural and forestry resources. *Nano Res.* **2022**, *15*, 7506–7532.

[30] Wang, R. L.; Chen, C. J.; Pang, Z. Q.; Wang, X. Z.; Zhou, Y. B.; Dong, Q.; Guo, M.; Gao, J. L.; Ray, U.; Xia, Q. Q. et al. Fabrication of cellulose-graphite foam via ion cross-linking and ambient-drying. *Nano Lett.* **2022**, *22*, 3931–3938.

[31] Guan, Q. F.; Yang, H. B.; Han, Z. M.; Ling, Z. C.; Yang, K. P.; Yin, C. H.; Yu, S. H. Plant cellulose nanofiber-derived structural material with high-density reversible interaction networks for plastic substitute. *Nano Lett.* **2021**, *21*, 8999–9004.

[32] Zhu, C. T.; Soldatov, A.; Mathew, A. P. Advanced microscopy and spectroscopy reveal the adsorption and clustering of Cu(II) onto tempo-oxidized cellulose nanofibers. *Nanoscale* **2017**, *9*, 7419–7428.

[33] Erlandsson, J.; Françon, H.; Marais, A.; Granberg, H.; Wågberg, L. Cross-linked and shapeable porous 3D substrates from freeze-linked cellulose nanofibrils. *Biomacromolecules* **2019**, *20*, 728–737.

[34] Lin, J. P.; Liu, J. R.; Zhang, K. X.; Deng, Y. L.; Che, W. R.; Pang, X. Y.; Zhang, Q. D.; Cai, W. Q.; Zeng, Z. H.; Wu, N. Ambient-pressure-dried aerogel amplifies interfacial polarization toward high-efficiency microwave absorption. *Adv. Funct. Mater.* **2025**, e20336.

[35] Zuo, T.; Zhang, J. W.; Xu, L.; Xu, T. Q.; Ren, W. J.; Liu, W. J.; Wang, T.; Wang, S. B.; Cai, Y.; Yi, L. M. Superhydrophobic cotton fabric based on aqueous paint for passive daytime radiative cooling. *Prog. Org. Coat.* **2024**, *190*, 108395.

[36] Li, L. H.; Liu, G. M.; Wei, S. C.; Zhang, Q.; Shi, R. D.; Wang, Y. J.; Wang, B.; Liu, Z.; Huang, K. N.; Wang, X. Y. et al. Facile synthesis of nickel ferrite decorated carbon nanotube/cellulose aerogel for efficient electromagnetic wave absorption. *Small Methods* **2025**, *9*, 2402260.

[37] Xie, X. B.; Wang, B. L.; Wang, Y. K.; Ni, C.; Sun, X. Q.; Du, W. Spinel structured MFe_2O_4 (M = Fe, Co, Ni, Mn, Zn) and their composites for microwave absorption: A review. *Chem. Eng. J.* **2022**, *428*, 131160.

[38] Liu, M. Z.; Wang, B.; Wang, Y. J.; Li, B. C.; Fu, D. X.; Chang, Y. F.; Chen, J. S.; Liu, K. R.; Han, Q.; Lu, X. D. et al. Synthesis of expanded microcrystalline graphite/$Mn_{0.4}Zn_{0.6}Fe_2O_4$ composites for electromagnetic wave absorption. *Chem. Eng. J.* **2025**, *521*, 166586.